PAPER

Check for updates

Few-layered CuInP$_2$S$_6$ nanosheet with sulfur vacancy boosting photocatalytic hydrogen evolution†

Peng Yu,[ab] Fengmei Wang, [ID] *[b] Jun Meng,[c] Tofik Ahmed Shifa,[b] Marshet Getaye Sendeku,[b] Ju Fang,[d] Shuxian Li,[d] Zhongzhou Cheng, [ID] [b] Xiaoding Lou [ID] *[a] and Jun He [ID] [b]

Photochemical water splitting offers an economic and sustainable approach for solar energy conversion into hydrogen fuel to mitigate the problem of greenhouse gas emissions. To this end, exploring novel semiconductor photocatalysts, which have efficient light absorption and thermodynamically favorable band alignment for water splitting, is crucial. Here, we rationally develop a new photocatalyst of CuInP$_2$S$_6$ nanosheets to generate hydrogen gas under light illumination. The CuInP$_2$S$_6$ nanosheet (with a thickness of around 4–7 nm) photocatalyst exhibits a high hydrogen production rate of 804 μmol g^{-1} h^{-1}, eight times higher than that of the microsheet counterpart, due to the introduced abundant sulfur vacancies. Experimental characterization and theoretical calculations verify that the prolonged carrier lifetime and optimized band alignment in ultrathin CuInP$_2$S$_6$ nanosheets boost photocatalytic hydrogen evolution. This work opens a new avenue for photocatalysis *via* using novel layered binary metal phosphorous trichalcogenides.

1. Introduction

The increased investment in renewable sources, such as solar power, provides a sustainable platform to mitigate the current challenges of energy demand and environmental conservation.[1] The direct production of clean fuels from sunlight provides a scalable route to realize efficient energy conversion. In this regard, solar-driven water splitting stands out among many solar fuel technologies owing to its sustainability and low cost.[2,3] The prerequisite for realizing an efficient photocatalytic water-splitting process relies on choosing the appropriate photocatalyst with suitable band alignment and electronic structure, ensuring effective light harvesting and enhancing carrier separation while withstanding photocorrosion in solutions.[4] To this end, earth-

abundant two-dimensional (2D) layered materials such as black phosphorus (BP),[5,6] graphitic carbon nitride (g-C$_3$N$_4$)[7,8] and transition metal dichalcogenides (TMDs)[9,10] have been developed as promising candidates in photocatalytic water splitting due to their appropriate bandgaps and tunable photoelectronic properties.[11] The newly emerging 2D layered metal phosphorous trichalcogenides (MPX$_3$) have been theoretically predicted and experimentally proved to be potential photocatalysts for water splitting.[12–15] They have many intriguing properties such as light responsiveness in a broad wavelength spectrum (350–950 nm),[16] high quantum yields,[12] and thermodynamically appropriate band edge positions.[17] In particular, the ultrathin 2D layered structure offers unique physical and chemical features:[18,19] (i) the coordinatively unsaturated surface atoms, combined with an ultra-high specific surface area, provides more active sites for catalytic reactions;[20,21] (ii) the few-layered thickness could effectively decrease the recombination of electron–hole pairs through shortening the migration distance from the interior to the surface;[12] (iii) the atomic vacancies could be easily introduced on the surface and serve as the charge separation centers to trap photogenerated electrons, preventing recombination with the photogenerated holes.[22,23]

Recently, we demonstrated the controllable synthesis of some ultrathin bivalent metal-based M^{II}PX$_3$ (where M^{II} = Mn, Fe, Ni) nanosheets for photocatalytic hydrogen generation and disclosed their mysterious property toward photocatalytic

[a] Engineering Research Center of Nano-Geomaterials of Ministry of Education, Faculty of Materials Science and Chemistry, China University of Geosciences, Wuhan 430074, China. E-mail: louxiaoding@cug.edu.cn
[b] CAS Center for Excellence in Nanoscience, CAS Key Laboratory of Nanosystem and Hierarchical Fabrication, National Center for Nanoscience and Technology, Beijing 100190, China. E-mail: wangfm@nanoctr.cn
[c] Division of Interfacial Water and Key Laboratory of Interfacial Physics and Technology, Shanghai Institute of Applied Physics, Chinese Academy of Sciences, Shanghai 201800, China
[d] School of Physics and Technology, Key Laboratory of Artificial Micro- and Nano-structures of Ministry of Education, Wuhan University, Wuhan, 430072, China
† Electronic supplementary information (ESI) available. See DOI: 10.1039/d0ce01487g

water splitting.[13,24,25] Of compelling interest in MPX_3 materials is that the bivalent metal could be substituted by univalent and trivalent metals to form layered $M^IM^{III}P_2X_6$ such that regulating the electronic structure and spin–orbit interactions would bring an interesting paradigm. The involvement of M^I and M^{III} cations could endow them with distinctive physical and chemical properties, unlike those of $M^{II}PX_3$.[26] The $CuInP_2S_6$ (CIPS) crystal,[27] as a specific representative, has exhibited intriguing properties including ferroelectric,[28] piezoelectric,[29] and pyroelectric[30] semiconducting characteristics. It consists of covalently bonded $[P_2S_6]^{4-}$ bipyramids in which the Cu, In, and P–P dimers are alternately arranged in a triangular pattern with strong intralayer bonding and weak interlayer van der Waals force (Fig. 1a). Recent studies show that ferroelectric spontaneous polarization could be recognized on the CIPS nanosheets at room temperature due to the Cu sites shifting off-center ordering along the z direction,[14,27,28,31] and this spontaneous polarization can induce a built-in electric field, which is helpful to drive the spatial separation of photogenerated charge carriers efficiently in photocatalytic reactions.[32,33] In addition, the formation energy of the sulfur vacancies in the CIPS monolayer (0.82 eV) is much lower than that in the MoS_2 monolayer (2.98 eV) due to the higher volatility of the chalcogenide at high temperature.[34,35] Therefore, the sulfur vacancies in CIPS are expected to be easily introduced during the chemical vapor conversion synthesis process. However, to our best knowledge, there are few reports about the study of its photocatalytic properties. This can be associated with a considerable challenge to controllably synthesize the $CuInP_2S_6$ nanosheets.

Here, we successfully develop an approach to controllably synthesize the sulfur-defective $CuInP_2S_6$ crystals, including nanosheets (NSs) and microsheets (MSs) *via* a facile chemical vapor conversion method. The as-obtained CIPS NSs and MSs are well crystallized and ascertained to be phase-pure. Based on experimental characterization and density functional

theory (DFT) calculations, we find that there is no obvious difference in the bandgaps, but the band alignment will be regulated after thinning down the CIPS crystal. Notably, the photogenerated carrier recombination rate could be suppressed on CIPS NSs with a prolonged carrier lifetime in CIPS NSs (3.25 ns) than MSs (2.26 ns) under light illumination. The introduced sulfur vacancies not only reduce the bandgap and then enhance light absorption but also regulate the charge distribution on the surface and optimize the charge carrier separation for effective photocatalytic reaction. Benefiting from the thermodynamically appropriate band alignment, shorter migration distance of carriers and abundant surface sulfur vacancies, the CIPS NSs demonstrated superior photocatalytic activity towards hydrogen generation. The hydrogen production rate of CIPS NSs is up to 804 μmol g^{-1} h^{-1}, outperforming that of CIPS MSs (100 μmol g^{-1} h^{-1}) and most of the reported 2D MPX_3 photocatalysts. This work provides a feasible route to synthesize the 2D $CuInP_2S_6$ crystal and explore its potential application as a photocatalyst for solar water splitting to produce hydrogen gas.

2. Experimental section

2.1. Chemical materials

All chemicals were analytical grade and used as received without further purification. Indium chloride tetrahydrate ($InCl_3\cdot4H_2O$), copper chloride dihydrate ($CuCl_2\cdot2H_2O$), thioacetamide (CH_3CSNH_2), ethylenediamine ($C_2H_8N_2$), anhydrous sodium sulfate (Na_2SO_4), anhydrous sodium sulfite (Na_2SO_3) and sodium sulfide nonahydrate ($Na_2S\cdot9H_2O$) were purchased from Aladdin. Red phosphorus and sulfur powder were purchased from Alfa Aesar. Deionized water with a conductivity of 18.25 MΩ cm was used as a solvent in all the experiments.

2.2. Material synthesis

A two-step process was used to prepare the $CuInP_2S_6$ sheets. In the first step, the $CuInS_x$ precursor was prepared through a solvothermal method. Then, the $CuInP_2S_6$ microsheets and nanosheets were prepared *via* the chemical vapor conversion reaction between the $CuInS_x$ precursor and the vapor source. The details are as follows.

Synthesis of $CuInS_x$ precursor. A solvothermal method was utilized to synthesize $CuInS_x$ nanocrystals.[36] Typically, a stoichiometric mixture of $CuCl_2\cdot2H_2O$ (0.1 mol L^{-1}), $InCl_3\cdot4H_2O$ (0.1 mol L^{-1}) and thioacetamide (0.3 mol L^{-1}) was dissolved in ethylenediamine (35 mL) under vigorous stirring. Then, the solution was transferred to a 50 mL Teflon-lined autoclave followed by heating at 160 °C for 12 h. After cooling to room temperature naturally, the products were collected by centrifugation at 5000 rpm for 5 min and washed with absolute ethanol three times. After that, the precipitate was dispersed in absolute ethanol and uniformly drop-casted on the surface of carbon fibers ($CuInS_x$/CFs). These carbon fibers were dried at 60 °C for the following step.
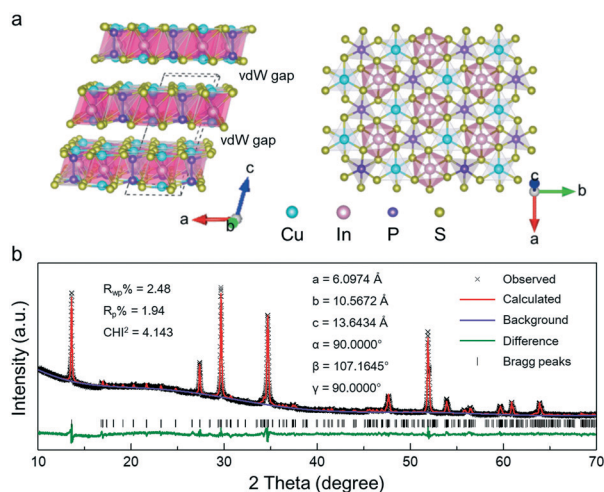

Fig. 1 (a) Side and top view of monoclinic CIPS crystal structure. (b) Rietveld refining XRD pattern for as-prepared CIPS MSs.

Synthesis of CIPS NSs and MSs. CIPS NSs and MSs were synthesized by a typical chemical vapor conversion reaction by employing a tube furnace with two zones (Fig. S2a†). Firstly, appropriate stoichiometric amounts of phosphorous and sulfur powders with the molar ratio of $n_P : n_S = 1 : 3$ were loaded in zone I of the furnace whereas the CuInS$_x$/CFs precursor was placed in zone II (the distance between the two zones is about 20 cm). Subsequently, the system was purged with Ar gas and vacuumed to create an air-free atmosphere. Before starting the reaction, the zone I and II were simultaneously heated to 300 °C and 510 °C (CIPS NSs) or 550 °C (CIPS MSs) within 30 min with continuously flowing 50 sccm Ar gas. The mixture of phosphorous and sulfur powders in zone I was finally heated to 320 °C and the reaction was run for 60 min (CIPS NSs) or 90 min (CIPS MSs). The detailed heating procedure profiles are shown in Fig. S2b and c.† When the reaction was completed, the furnace was naturally cooled to room temperature and the samples were taken out for further measurements. The mass loading of CIPS NSs and MSs on the CFs is about 3.2 and 5.6 mg cm^{-2}, respectively.

2.3. Material characterization

The morphology and thickness of CuInP$_2$S$_6$ sheets were investigated by field emission scanning electron microscopy (SEM, Hitachi S4800) and atomic force microscopy (AFM, Bruker-M8). The crystal structure and chemical compositions were identified by transmission electron microscopy (TEM, JEM-2100F) and energy dispersive X-ray spectroscopy (EDX) equipped on a JEM-2100F instrument. An X-ray diffractometer (XRD, Smartlab-9) equipped with Cu Kα radiation was used to confirm the crystal structure with a scanning speed of 2° min^{-1}. Raman spectra were determined using a confocal microscope-based Raman spectrometer (Renishaw InVia) under ambient conditions with an excitation laser wavelength of 532 nm. Room temperature UV-vis diffuse reflectance spectra with the wavelength range of 200–1000 nm were recorded on a Lambda 750 spectrophotometer. Ultraviolet photoelectron spectroscopy (UPS, Thermo Scientific ESCALab220Xi-XL) was used to analyze the valence band energy of CuInP$_2$S$_6$ sheets. X-ray photoelectron spectroscopy (XPS, Thermo Scientific ESCALab250Xi) was performed using a Mg Kα source excited at 8 kV and the analysis chamber pressure was 1.5×10^{-9} Mbar. Electron spin resonance (ESR, Bruker E500) spectroscopy was carried out to detect the vacancies of samples and the radical of the photocatalytic process. Time-resolved photoluminescence (TRPL, NanoLOG-TCSPC) spectroscopy was conducted to examine the electron transfer dynamics of CuInP$_2$S$_6$.

2.4. Electrochemical measurement

A typical three-electrode system was used to conduct the Mott–Schottky and electrochemical impedance spectroscopy (EIS) measurements on a Princeton Applied Research (VersaSTAT3) potentiostat. A piece of CIPS/CFs (1 × 2 cm^2)

was directly used as the working electrode, with a Pt wire as a counter electrode and a saturated calomel electrode (SCE) as the reference electrode in 0.5 M Na$_2$SO$_4$ aqueous electrolyte (pH 6.8). The Mott–Schottky analysis was performed at the frequency of 500 and 2500 Hz. EIS measurement was carried out under an open circuit potential with the frequency ranging from 100 000 to 0.1 Hz. During the photoelectrochemical measurements, the CIPS sheets were transferred onto fluorine-doped tin oxide (FTO) conductive glass slides that served as a working electrode. Typically, CIPS MS and NS suspension solution were cast onto the surface of conductive FTO glass and then covered by epoxy resin to ensure an exposed area of 0.4 cm × 0.5 cm. The photocurrent responses of the different electrodes were achieved under Xe lamp light ($\lambda > 300$ nm) illumination, and the distance between the Xe lamp and the working electrode was 20 cm with the light power density of 200 mW cm^{-2}. All the potentials reported here were converted to normal hydrogen electrode (NHE) through the equation: E (vs. NHE) = E (vs. SCE) + 0.242 V.

2.5. Photocatalytic H$_2$ evolution

Prior to the experiment, the CIPS NS suspension solution (0.05 mg mL^{-1}, 100 mL) was obtained through sonication of CIPS sheets from carbon fibers in deionized water. Then, 0.1 mol L^{-1} Na$_2$S/Na$_2$SO$_3$ was added into this suspension solution and acted as a sacrificial agent. The reaction was conducted in a Pyrex top-irradiation photoreactor connected to a glass closed gas circulation system. A 300 W Xe lamp ($\lambda > 300$ nm) was utilized as the light source, and the distance between the Xe lamp and the liquid surface of the photoreactor is 10 cm with a light power density of 400 mW cm^{-2}. Before turning on the light, the aqueous solution was carefully evacuated to remove the air in this sealed system. The generated H$_2$ gas was online detected using GC-7900 gas chromatograph (GC, TCD detector, 5 Å molecular sieve column and Ar as a carrier gas) at hourly intervals. Meanwhile, in order to ensure uniform catalyst dispersion and gas release, the solution was subjected to stirring.

2.6. Computational details

All the CuInP$_2$S$_6$ structures are built according to the lattice parameters from the experimental XRD measurement results. A vacuum layer of 15 Å is employed for the monolayer structure to prevent interactions between the repeated slabs. All the calculations are performed based on density functional theory (DFT) implemented in the Vienna Ab initio Simulation Package (VASP).[37] The structures are fully relaxed by the projector-augmented wave (PAW) potentials[38] and the Perdew–Burke–Ernzerhof (PBE) exchange–correlation functional based on the GGA approximation.[39] The DFT-D3 method including the dispersion correction proposed by Grimme[40] is applied to describe the van der Waals interactions between the CuInP$_2$S$_6$ layers. The cutoff energy of the plane wave is 400 eV. The convergence of the electronic

self-consistent energy is 10^{-4} eV, and the force convergence criterion in a conjugate-gradient algorithm is 0.05 eV/Å. The electronic structures are calculated using the Heyd–Scuseria–Ernzerhof (HSE06) hybrid functional.[41] All the calculations are spin-polarized.

3. Results and discussion

3.1. Synthesis and structural characterization

The CIPS NSs and MSs were synthesized by a two-step process, in which the CuInS$_x$ precursor was first synthesized *via* a solvothermal method[36] (Fig. S1†) and afterwards the as-obtained precursor was converted to the well-crystallized CIPS sheets on the carbon fiber *via* chemical vapor conversion (Fig. S2†). The morphology of 2D CIPS crystals can be tuned by controlling the reaction time and temperature during the second step. Fig. S3† shows the scanning electron microscopy (SEM) images of the various CIPS sheets on the surface of the carbon fiber substrate. Uniform CIPS NSs and MSs could be synthesized within 60 min at 510 °C and 90 min at 550 °C, respectively. The crystal structure of the as-synthesized 2D CIPS sheets was first characterized by X-ray diffraction (XRD) and then refined by the Rietveld method using General Structure Analysis System (GSAS) software. As shown in Fig. 1b, the typical diffraction peaks can be clearly indexed to the monoclinic CIPS phase with a space group of *Cc* and lattice parameters of $a = 6.0974$ Å, $b = 10.5672$ Å, $c = 13.6434$ Å and $\beta = 107.1645°$. The final refined reliability factors indicate the formation of pure-phase CIPS without other detectable crystalline impurities. The SEM images (Fig. 2a and S4a–c†) show the vertically grown CIPS NSs with an average size of ~1 μm on the carbon fibers. The thickness of the CIPS NSs is around 4–7 nm (inset of Fig. 2a) based on atomic force microscopy (AFM) characterization. We then applied transmission electron microscopy (TEM) to investigate the structural characteristics (Fig. 2b). The interplanar lattice spacings of 3.01 and 2.91 Å in the high-resolution TEM (HRTEM, Fig. 2c) image are indexed to the (130) and (200) facets of the CIPS crystal, respectively. The corresponding selected area electron diffraction (SAED, inset of Fig. 2c and S5†) pattern unequivocally discloses a single set of diffraction spots, consisting of a CIPS unit cell with its lattice constant. Energy-dispersive X-ray spectroscopy (EDX) mapping (Fig. 2d) verified the uniform elemental distribution of Cu, In, P and S with the atomic ratio of 1:1:1.8:5. As a comparison, the CIPS MSs were also characterized. There is no difference in the crystal structure of CIPS NSs and MSs (Fig. S6†), but the lateral size of the CIPS MSs is around 10 μm with the Cu:In:P:S ratio of 1:1.1:2.2:6.3 and thickness of about 700 nm (Fig. S7†).

To gain insight into the elemental chemical state information, we conducted X-ray photoelectron spectroscopy (XPS) analysis of the CIPS crystals (Fig. S8†). The high-resolution XPS spectra of different elements in both CIPS NSs and MSs are very close to each other (Fig. 2e). The peak pairs located at around 952.39 ($2p_{1/2}$)/932.65 ($2p_{3/2}$) eV and 452.47 ($3d_{3/2}$)/444.91 ($3d_{5/2}$) eV are indexed to Cu$^+$ and In^{3+} species, respectively. The peaks at 132.54 ($2p_{1/2}$) and 131.65 eV ($2p_{3/2}$) correspond to P^{4+}, while those at 163.33 ($2p_{1/2}$) and 162.13 eV ($2p_{3/2}$) belong to S^{2-} in the P$_2$S$_6$ unit. After carefully comparing the high-resolution Cu 2p, In 3d, P 2p and S 2p XPS spectra in both CIPS MSs and NSs, we found that the binding energies, especially S 2p, in CIPS NSs slightly shift to lower values compared with those in CIPS MSs due to the existence of abundant sulfur vacancies.[42,43] Additionally, electron spin resonance (ESR) spectroscopy was carried out to further verify the sulfur vacancies (Fig. S9†). The clear ESR signal at $g = 2.003$ of CIPS samples could be attributed to the unpaired electrons on the sulfur atoms of sulphide,[44,45] also suggesting the existence of sulfur vacancies in the CIPS MSs and NSs. The higher ESR intensity of CIPS NSs indicates many more sulfur vacancies, which is in agreement with the XPS results. Raman spectra collected on both CIPS NSs and MSs show two vibration modes of zwitterion and the P$_2$S$_6$ unit with D_{3d} symmetry (Fig. S10†).[46] The vibration peaks between the anion [P$_2$S$_6$]$^{4-}$ and the cations (Cu$^+$ and In^{3+}) appear at 102.3, 116.8 and 315.2 cm^{-1}, respectively. A small peak at around 162 cm^{-1} is designated as the infrared-active E$_u$ mode of the P$_2$S$_6$ unit, which is observed in most of the layered MPX$_3$ materials.[47] In addition, other vibration peaks, including E$_g$ (216 and 264 cm^{-1}) and A$_{1g}$ (239, 375 and 448 cm^{-1}), are ascribed to the four vibration modes ([P–S], [P–P], [S–P–S] and [S–P–P]) of the P$_2$S$_6$ unit,[46] and the E$_g$ and A$_{1g}$ modes represent the tangential (in-plane) and stretching (out-of-plane) vibrations of the P–P bond in the P$_2$S$_6$ unit, respectively.
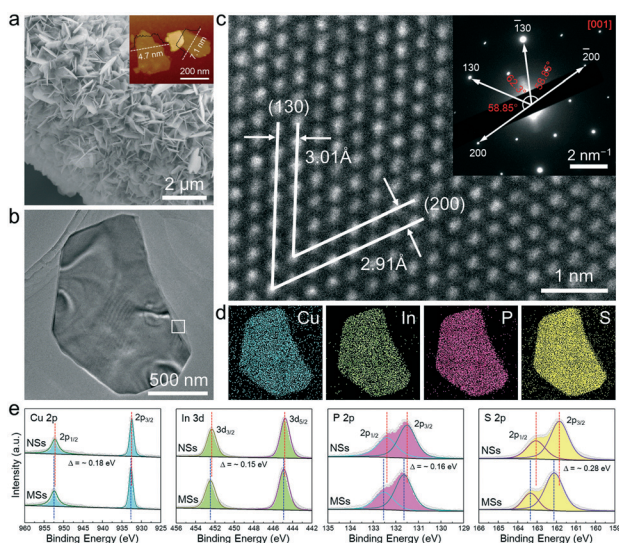

Fig. 2 (a) SEM image of the as-prepared CIPS NSs on the carbon fibers. Inset: AFM image with the thickness of CIPS NSs. (b–d) TEM (b) and HRTEM (c) images and EDX elemental mapping (d) of single CIPS nanosheet. Inset of (c): SAED pattern collected from the marked region in (b). (e) XPS high-resolution scans of Cu 2p, In 3d, P 2p and S 2p regions in the CIPS NSs and MSs.
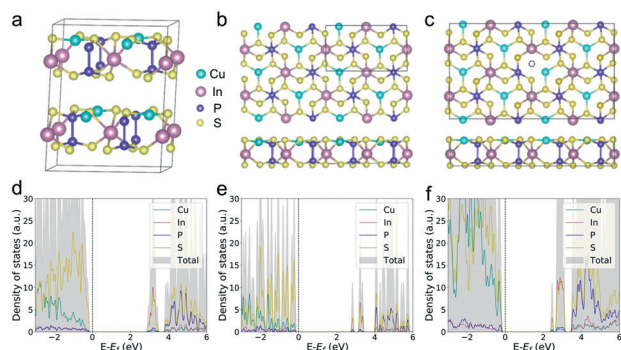
Fig. 3 (a–c) The crystal structures of CIPS bulk (a), CIPS monolayer (b), and S defective CIPS monolayer (c). The S vacancy is marked by a dashed-line circle in (c). (d–f) Corresponding total projected density of states (PDOS) of the CIPS bulk (d), CIPS monolayer (e) and S defective CIPS monolayer (f). The Fermi energy levels are set as 0 eV.

3.2. DFT calculations

Given the aforementioned characterization of thick (>700 nm) and ultrathin (<7 nm) CIPS sheets, density functional theory (DFT) calculations were firstly employed to elucidate the electronic structure of the bulk and monolayered CIPS (Fig. 3a and b). The density of states (DOS) calculated *via* HSE06 methods reveal bandgap values of the bulk and monolayered CIPS of 3.02 eV and 2.88 eV, respectively, indicating that the bandgap is reduced by 0.14 eV when the thickness of CIPS is brought down to a monolayer. This result suggests that the bandgap of the CIPS is not strongly dependent on the layer numbers. In addition, the effect of the S vacancies on the electronic structure is also studied (Fig. 3c). After introducing S vacancies in the CIPS monolayer, shallow trap states are induced near the conduction band, resulting in a narrowed bandgap of 2.52 eV. The reduced bandgap may facilitate the photoexcitation of the electron in a broadened spectral range. As revealed in the projected density of states (PDOS) of the stoichiometric CIPS bulk and monolayer (Fig. 3d and e), the valence band maximum (VBM) mainly consists of the S 3p, and the conduction band minimum (CBM) is composed of S 3p and In 3d orbitals. In contrast, for the CIPS monolayer with S vacancies, the VBM mainly consists of the P 3p and Cu 3p orbitals (Fig. 3f). The emerging contribution of the Cu-3p orbital near the Fermi level suggests that more electrons can be easily photoexcited and further indicates that the S vacancies could improve photo-absorption. More importantly, the introduced S vacancies give rise to the charge redistribution on the surface with charge accumulation on the adjacent P atom (Fig. S11†), which may provide more active sites for photocatalytic reaction on the CIPS.

3.3. Optical characteristics

To evaluate the light-harvesting capability of the CIPS MSs and NSs through experiment, UV-vis diffuse reflectance spectroscopy (DRS) measurement was performed (Fig. 4a). The absorption edges of CIPS NSs and MSs are close to each
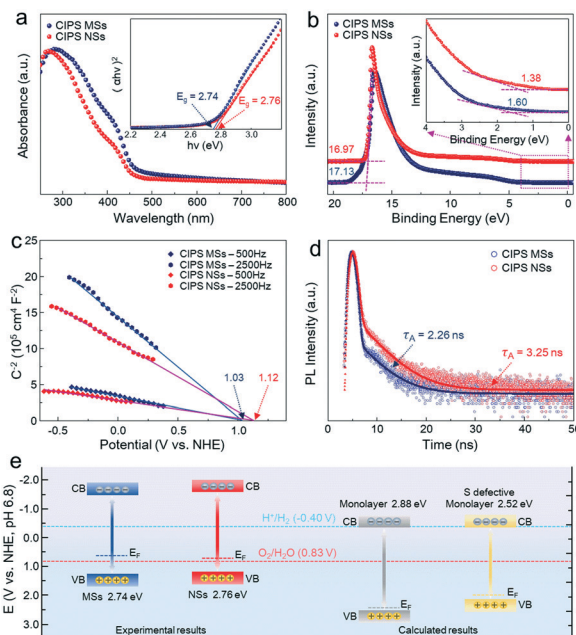

Fig. 4 (a) UV-vis diffuse reflectance spectra of CIPS MSs and NSs. Inset: Tauc plots for the determination of bandgaps, the obtained bandgaps estimated by $(\alpha h v)^2$ as a function of hv, where α and v are the absorbance and wavenumber, respectively. (b) UPS spectra of CIPS MSs and NSs. (c) Mott–Schottky plots collected on the CIPS MS and NS electrodes at 500 and 2500 Hz in 0.5 M Na_2SO_4. (d) Time-resolved PL spectra of CIPS MSs and NSs with the excitation wavelength of 320 nm. (e) Band alignment diagram of CIPS MS and NS samples (left) and the theoretically calculated results of the CIPS monolayer without and with S vacancies (right).

other, from which the bandgaps of 2.76 eV and 2.74 eV can be extracted *via* the Kubelka–Munk function. Ultraviolet photoelectron spectroscopy (UPS) was further adopted to investigate the energy level of the valence band maximum (E_{VB}). By subtracting the width of the He I UPS spectra (Fig. 4b) from the excitation energy (21.22 eV), the E_{VB} could be calculated to be −5.63 eV *vs.* vacuum level (*i.e.*, 1.19 V *vs.* NHE) and −5.69 eV *vs.* vacuum level (*i.e.*, 1.25 V *vs.* NHE) for CIPS NSs and MSs, respectively. Combined with the bandgaps, the corresponding conduction band minimum (E_{CB}) was calculated to be −2.87 eV *vs.* vacuum level (*i.e.*, −1.57 V *vs.* NHE) and −2.95 eV *vs.* vacuum level (*i.e.*, −1.49 V *vs.* NHE) by $E_{VB} - E_g$. These results clearly show that the band-edge positions of CIPS MSs and NSs are slightly different, which are probably attributed to the changed surface states and thickness,[48] even if there is no big difference in the bandgap values. The Mott–Schottky (M–S) plots measured on the as-synthesized CIPS samples show negative slopes, suggesting a typical p-type semiconductor characteristic for CIPS (Fig. 4c).[49] By extending the asymptotic curve of the M–S plots, the intersection points with the X-axis ($1/C^2 = 0$) can determine the flat-band potential (E_{fb}) values, which are 1.03 and 1.12 V *vs.* NHE for CIPS MSs and NSs, respectively. Actually, based on the flat-band potential value, which is the difference between the

Fermi level (E_F) and the water-reduction potential (*i.e.*, −0.4 V *vs.* NHE at pH 6.8),[50] the Fermi level can be estimated to be 0.63 and 0.72 V *vs.* NHE for CIPS MSs and NSs, respectively. The band alignment, combined with the standard energy position of H^+/H_2 and H_2O/O_2 redox pairs (Fig. 4e, left), indicates the thermodynamic appropriateness for photocatalytic water splitting under light illumination. The theoretical results based on the CIPS monolayer without and with S vacancies are also presented (Fig. 4e, right), showing a p-type semiconductor and the higher position of E_{CB} than the H^+/H_2 redox potential.

For further study of the charge carrier (*i.e.*, photogenerated electron–hole pairs) separation and transfer properties of the semiconductor photocatalyst, steady-state and time-resolved spectroscopic techniques were applied. As shown in Fig. S12,† there is no obvious change in the photoluminescence (PL) spectra of CIPS MSs and NSs except for the intensity. Compared with the PL spectrum of CIPS MSs, the intensity of the CIPS NS PL spectrum sharply diminished, suggesting that carrier recombination was effectively hindered. In addition, time-resolved photoluminescence (TRPL) spectra were recorded to examine the lifetime of photogenerated carriers. The TRPL curves were obtained by exponential decay kinetics function fitting (Table S1†):[51]

$$I(t) = A_1 \exp(-t/\tau_1) + A_2 \exp(-t/\tau_2) \tag{1}$$

Meanwhile, the average lifetime (τ_A) could be calculated through the following equation:

$$\tau_A = (A_1\tau_1^2 + A_2\tau_2^2)/(A_1\tau_1 + A_2\tau_2) \tag{2}$$

where A_1 and A_2 are the amplitudes, and τ_1 and τ_2 correspond to the short and long fluorescent lifetime, respectively. The short lifetime τ_1 is attributed to the non-radiative recombination of the photogenerated electron–hole pairs on the surface of photocatalysts. The long lifetime τ_2 is ascribed to the inter-band recombination of free excitons.[51] Significantly, A_1 is much larger than A_2 in CIPS NSs and MSs, indicating that the short lifetime τ_1 is predominant. The τ_1 of CIPS NSs is longer than that of CIPS MSs, corroborating the longer charge carrier lifetime on the surface of CIPS NSs such that the CIPS NS photocatalysts shows an increased average lifetime (τ_A) of 3.25 ns than that (2.26 ns) of CIPS MSs (Fig. 4d), indicating that the ultrathin 2D feature of CIPS NSs could suppress the charge recombination and thus elongate the lifetime of the photogenerated charge carriers. The photoresponse current (Fig. 5a) of the different electrodes under the same light irradiation (200 mW cm^{-2}) further confirm the decreased recombination rate of photogenerated electron–hole pairs on the CIPS NS photoelectrode. The photocurrent of 2.9 μA cm^{-2}, near threefold higher than that of CIPS MS (1.1 μA cm^{-2}), is produced on the CIPS NS electrode. Electrochemical impedance spectroscopy (EIS) measurements under the open-circuit potential also provided
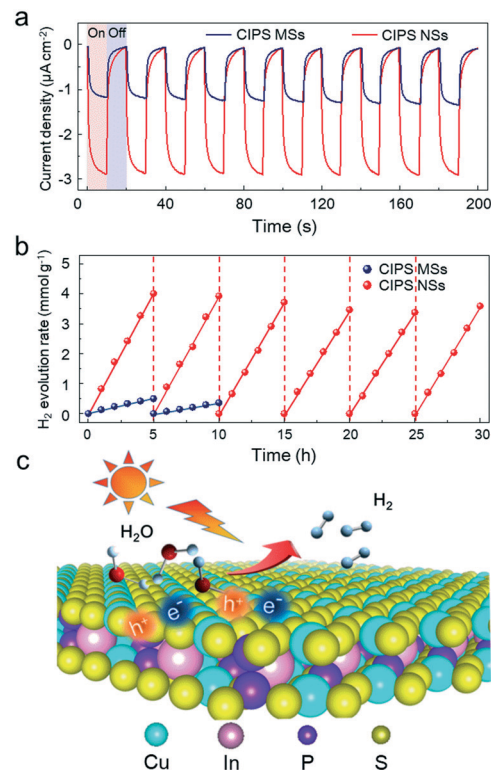
Fig. 5 (a) Transient photocurrent responses of CIPS MS and NS photoelectrodes with the size of 1 cm × 2 cm under Xe light illumination ($\lambda > 300$ nm, 200 mW cm^{-2}). (b) Comparison of photocatalytic hydrogen evolution performance of CIPS MSs and NSs under Xe light illumination ($\lambda > 300$ nm, 400 mW cm^{-2}). (c) Schematic for the photocatalytic hydrogen evolution on the CIPS NSs.

evidence that CIPS NSs have faster charge transfer with lower resistance (Fig. S13†). These results firmly manifest that efficient separation and transfer of photogenerated electron–hole pairs can be realized on CIPS NS. In short, the CIPS NSs can provide much more superficial active sites and shorten the diffusion paths of photogenerated carriers from the interior to the surface during catalytic reactions. In contrast, the thick CIPS MSs are unfavorable for photocatalytic reactions due to the longer diffusion distance and the easy recombination of electron–hole pairs.

3.4. Photocatalytic evolution of H_2

Based on the aforementioned results, we evaluated the photocatalytic hydrogen evolution activity of these two CIPS samples in aqueous solution containing Na_2S/Na_2SO_3 as the sacrificial electron donor under illumination of xenon light ($\lambda > 300$ nm, 400 mW cm^{-2}). As expected, the CIPS NS photocatalyst shows an efficient hydrogen production rate of ~804 μmol g^{-1} h^{-1} (Fig. 5b) which is much higher than that of the CIPS MSs photocatalyst (100 μmol g^{-1} h^{-1}). In addition, it outperforms the 2D MPX_3 photocatalysts reported to date (Table S2†) and is even comparable to other 2D layered photocatalysts (Table S3†). Then, we studied the stability of the photocatalyst through continuous hydrogen generation

under the same conditions for 30 h (Fig. 5b). Notably, CIPS NSs demonstrate excellent stability. The relatively improved photocatalytic activity of CIPS NSs, compared with CIPS MSs, can be attributed to the ultrathin 2D feature and abundant surface sulfur vacancies, which result in an increase in reactive sites and prolonged lifetime of photogenerated carriers. In addition, CIPS NSs exhibited a considerable photocatalytic H$_2$ evolution rate of 46 μmol g^{-1} h^{-1} and reasonable stability in pure water without any sacrificial agent under the same illumination conditions (Fig. S14†). Unfortunately, there is no detectable oxygen gas in the experimental protocol without applying any sacrificial agent. After further characterization, the unchanged morphology and structural crystal (Fig. S15†), along with the slightly oxidized surface, of the CIPS NSs are observed after long-term operation (Fig. S16†). We employed *in situ* ESR spectroscopy analysis to track the radicals of hydroxyl moieties (˙OH) in the way of oxygen evolution (Fig. S17†). Accordingly, the ESR signal evidences the presence of ˙OH, substantiating the fact that the OER route is at the stage of primary oxidation on the adsorbed water molecule (H$_2$O − e$^-$ → ˙OH).

4. Conclusions

2D vdW CuInP$_2$S$_6$ nanosheets and microsheets are initially prepared by effectively controlling the synthesis parameters in a two-step process. The S vacancies can be introduced in the CuInP$_2$S$_6$ during this synthetic method. Based on theoretical calculations and experimental characterization, we find that the thickness and sulfur vacancies of the CuInP$_2$S$_6$ can affect the band-edge positions, even though there is no obvious change in bandgap value. Meanwhile, benefitting from the ultrathin features and abundant sulfur vacancies, CuInP$_2$S$_6$ nanosheets demonstrate an excellent photocatalytic hydrogen generation due to efficient separation of photogenerated carriers and high specific surface area. We found a high rate of hydrogen production activity for CuInP$_2$S$_6$ nanosheets (804 μmol g^{-1} h^{-1}), which is eightfold higher than that of CuInP$_2$S$_6$ microsheets. This work not only provides a facile synthesis of 2D CuInP$_2$S$_6$ but also demonstrates the promising application of layered M^I-M^{III}P$_2$X$_6$ materials to utilize solar energy and thereby generate clean fuels.

Conflicts of interest

There are no conflicts to declare.

Acknowledgements

References

1 N. S. Lewis, *Science*, 2016, **351**, 1920.

2 G. Han and Y. Sun, *Nat. Energy*, 2019, **4**, 532–533.

3 Z. Wang, Y. Inoue, T. Hisatomi, R. Ishikawa, Q. Wang, T. Takata, S. Chen, N. Shibata, Y. Ikuhara and K. Domen, *Nat. Catal.*, 2018, **1**, 756–763.

4 P. Ganguly, M. Harb, Z. Cao, L. Cavallo, A. Breen, S. Dervin, D. D. Dionysiou and S. C. Pillai, *ACS Energy Lett.*, 2019, **4**, 1687–1709.

5 B. Tian, B. Tian, B. Smith, M. C. Scott, R. Hua, Q. Lei and Y. Tian, *Nat. Commun.*, 2018, **9**, 1397.

6 M. Zhu, S. Kim, L. Mao, M. Fujitsuka, J. Zhang, X. Wang and T. Majima, *J. Am. Chem. Soc.*, 2017, **139**, 13234–13242.

7 Q. Han, B. Wang, J. Gao, Z. Cheng, Y. Zhao, Z. Zhang and L. Qu, *ACS Nano*, 2016, **10**, 2745–2751.

8 Y. Yu, W. Yan, X. Wang, P. Li, W. Gao, H. Zou, S. Wu and K. Ding, *Adv. Mater.*, 2018, **30**, 1705060.

9 P. Wang, Y. Mao, L. Li, Z. Shen, X. Luo, K. Wu, P. An, H. Wang, L. Su, Y. Li and S. Zhan, *Angew. Chem.*, 2019, **131**, 11451–11456.

10 D. Wang, H. Zeng, X. Xiong, M. F. Wu, M. Xia, M. Xie, J. P. Zou and S.-L. Luo, *Sci. Bull.*, 2020, **65**, 113–122.

11 D. Deng, K. S. Novoselov, Q. Fu, N. Zheng, Z. Tian and X. Bao, *Nat. Nanotechnol.*, 2016, **11**, 218.

12 X. Zhang, X. Zhao, D. Wu, Y. Jing and Z. Zhou, *Adv. Sci.*, 2016, **3**, 1600062.

13 T. A. Shifa, F. Wang, Z. Cheng, P. He, Y. Liu, C. Jiang, Z. Wang and J. He, *Adv. Funct. Mater.*, 2018, **28**, 1800548.

14 F. Wang, T. A. Shifa, P. Yu, P. He, Y. Liu, F. Wang, Z. Wang, X. Zhan, X. Lou, F. Xia and J. He, *Adv. Funct. Mater.*, 2018, **28**, 1802151.

15 X. Zhan, F. Wang, Z. Cheng, Z. Wang and J. He, *Sci. Bull.*, 2019, **64**, 958–960.

16 K. Z. Du, X. Z. Wang, Y. Liu, P. Hu, M. I. B. Utama, C. K. Gan, Q. Xiong and C. Kloc, *ACS Nano*, 2016, **10**, 1738–1743.

17 M. A. Susner, M. Chyasnavichyus, M. A. McGuire, P. Ganesh and P. Maksymovych, *Adv. Mater.*, 2017, **29**, 1602852.

18 C. Tan, X. Cao, X. J. Wu, Q. He, J. Yang, X. Zhang, J. Chen, W. Zhao, S. Han, G. H. Nam, M. Sindoro and H. Zhang, *Chem. Rev.*, 2017, **117**, 6225–6331.

19 Y. Song, H. Wang, J. Xiong, B. Guo, S. Liang and L. Wu, *Appl. Catal., B*, 2018, **221**, 473–481.

20 T. A. Shifa and A. Vomiero, *Adv. Energy Mater.*, 2019, **9**, 1902307.

21 Q. Fu, T. Wu, G. Fu, T. Gao, J. Han, T. Yao, Y. Zhang, W. Zhong, X. Wang and B. Song, *ACS Energy Lett.*, 2018, **3**, 1744–1752.

22 J. Di, J. Xia, M. F. Chisholm, J. Zhong, C. Chen, X. Cao, F. Dong, Z. Chi, H. Chen, Y. X. Weng, J. Xiong, S. Z. Yang, H. Li, Z. Liu and S. Dai, *Adv. Mater.*, 2019, **31**, 1807576.

23 F. Bai, L. Xu, X. Zhai, X. Chen and W. Yang, *Adv. Energy Mater.*, 2019, 1902107.

24 Z. Cheng, T. A. Shifa, F. Wang, Y. Gao, P. He, K. Zhang, C. Jiang, Q. Liu and J. He, *Adv. Mater.*, 2018, **30**, 1707433.

25 F. Wang, T. A. Shifa, P. He, Z. Cheng, J. Chu, Y. Liu, Z. Wang, F. Wang, Y. Wen, L. Liang and J. He, *Nano Energy*, 2017, **40**, 673–680.

26 M. I. Alonso, K. Wakita, J. Pascual, M. Garriga and N. Yamamoto, *Phys. Rev. B: Condens. Matter Mater. Phys.*, 2001, **63**, 075203.

27 A. Simon, J. Ravez, V. Maisonneuve, C. Payen and V. B. Cajipe, *Chem. Mater.*, 1994, **6**, 1575–1580.

28 F. Liu, L. You, K. L. Seyler, X. Li, P. Yu, J. Lin, X. Wang, J. Zhou, H. Wang, H. He, S. T. Pantelides, W. Zhou, P. Sharma, X. Xu, P. M. Ajayan, J. Wang and Z. Liu, *Nat. Commun.*, 2016, **7**, 12357.

29 V. Samulionis, J. Banys, A. Dziaugys, M. I. Gurzan, I. P. Pritz and Y. U. Vysochanskii, *Ferroelectrics*, 2011, **419**, 97–102.

30 L. Niu, F. Liu, Q. Zeng, X. Zhu, Y. Wang, P. Yu, J. Shi, J. Lin, J. Zhou, Q. Fu, W. Zhou, T. Yu, X. Liu and Z. Liu, *Nano Energy*, 2019, **58**, 596–603.

31 V. Maisonneuve, V. Cajipe, A. Simon, R. Von Der Muhll and J. Ravez, *Phys. Rev. B: Condens. Matter Mater. Phys.*, 1997, **56**, 10860.

32 F. Chen, H. Huang, L. Guo, Y. Zhang and T. Ma, *Angew. Chem., Int. Ed.*, 2019, **58**, 10061–10073.

33 L. Ju, J. Shang, X. Tang and L. Kou, *J. Am. Chem. Soc.*, 2019, **142**, 1492–1500.

34 J. Y. Noh, H. Kim and Y. S. Kim, *Phys. Rev. B: Condens. Matter Mater. Phys.*, 2014, **89**, 205417.

35 Z. Z. Sun, H. Huang, W. Xun, S. Shi, X. Hao, S. Ju and Y. Z. Wu, *J. Phys.: Condens. Matter*, 2020, **32**, 33.

36 W. C. Huang, C. H. Tseng, S. H. Chang, H. Y. Tuan, C. C. Chiang, L. M. Lyu and M. H. Huang, *Langmuir*, 2012, **28**, 8496–8501.

37 G. Kresse and J. Hafner, *Phys. Rev. B: Condens. Matter Mater. Phys.*, 1993, **47**, 558.

38 P. E. Blöchl, O. Jepsen and O. K. Andersen, *Phys. Rev. B: Condens. Matter Mater. Phys.*, 1994, **49**, 16223.

39 J. P. Perdew, J. A. Chevary, S. H. Vosko, K. A. Jackson, M. R. Pederson, D. J. Singh and C. Fiolhais, *Phys. Rev. B: Condens. Matter Mater. Phys.*, 1992, **46**, 6671.

40 S. Grimme, J. Antony, S. Ehrlich and H. Krieg, *J. Chem. Phys.*, 2010, **132**, 154104.

41 J. Heyd, G. E. Scuseria and M. Ernzerhof, *J. Chem. Phys.*, 2003, **118**, 8207–8215.

42 X. Sun, X. Luo, X. Zhang, J. Xie, S. Jin, H. Wang, X. Zheng, X. Wu and Y. Xie, *J. Am. Chem. Soc.*, 2019, **141**, 3797–3801.

43 H. Li, C. Tsai, A. L. Koh, L. Cai, A. W. Contryman, A. H. Fragapane, J. Zhao, H. S. Han, H. C. Manoharan and F. Abild-Pedersen, *Nat. Mater.*, 2016, **15**, 48–53.

44 L. Li, Z. Qin, L. Ries, S. Hong, T. Michel, J. Yang, C. Salameh, M. Bechelany, P. Miele, D. Kaplan, M. Chhowalla and D. Voiry, *ACS Nano*, 2019, **13**, 6824–6834.

45 S. Zhang, X. Liu, C. Liu, S. Luo, L. Wang, T. Cai, Y. Zeng, J. Yuan, W. Dong and Y. Pei, *ACS Nano*, 2018, **12**, 751–758.

46 Y. M. Vysochanskii, V. A. Stephanovich, A. A. Molnar, V. B. Cajipe and X. Bourdon, *Phys. Rev. B: Condens. Matter Mater. Phys.*, 1998, **58**, 9119–9124.

47 M. Scagliotti, M. Jouanne, M. Balkanski, G. Ouvrard and G. Benedek, *Phys. Rev. B: Condens. Matter Mater. Phys.*, 1987, **35**, 7097–7104.

48 J. Jasieniak, M. Califano and S. E. Watkins, *ACS Nano*, 2011, **5**, 5888–5902.

49 H. S. Park, K. E. Kweon, H. Ye, E. Paek, G. S. Hwang and A. J. Bard, *J. Phys. Chem. C*, 2011, **115**, 17870–17879.

50 B. A. Pinaud, Z. Chen, D. N. Abram and T. F. Jaramillo, *J. Phys. Chem. C*, 2011, **115**, 11830–11838.

51 C. Du, B. Yan, Z. Lin and G. Yang, *J. Mater. Chem. A*, 2020, **8**, 207–217.